Energy Storage

WILEY

ENERGY STORAGE

RESEARCH ARTICLE OPEN ACCESS

Lattice Boltzmann Simulation of Lauric Acid Melting in Rectangular Cavity With Different Fin Configurations With OpenLB

Alexandre de Quadro Tacques Filho[1,2] | Tim Niklas Bingert[3,4] | Adrian Kummerländer[3,4] | Luiz Eduardo Czelusniak[4] | Mathias J. Krause[3,4] | Márcio Dorn[1,2,5]

[1]Institute of Informatics, Federal University of Rio Grande do Sul, Porto Alegre, Rio Grande do Sul, Brazil | [2]Laboratory of Structural Bioinformatics and Computational Biology, Federal University of Rio Grande do Sul, Porto Alegre, Rio Grande do Sul, Brazil | [3]Institute for Mechanical Process Engineering and Mechanics, Karlsruhe Institute of Technology, Karlsruhe, Baden-Württemberg, Germany | [4]Lattice Boltzmann Research Group, Karlsruhe Institute of Technology, Karlsruhe, Baden-Württemberg, Germany | [5]Center for Biotechnology, Federal University of Rio Grande Do Sul, Porto Alegre, Rio Grande do Sul, Brazil

Correspondence: Márcio Dorn (mdorn@inf.ufrgs.br)

Received: 24 April 2025 | **Revised:** 8 July 2025 | **Accepted:** 16 July 2025

Funding: This work was supported by Fundação de Amparo à Pesquisa do Estado do Rio Grande do Sul, 24/2551-0001392-0, 23/2551-0001894-2. Conselho Nacional de Desenvolvimento Científico e Tecnológico, 314082/2021-2, 408154/2022-5, 440279/2022-4, 404319/2024-6, and 309465/2025-7. Coordenação de Aperfeiçoamento de Pessoal de Nível Superior. Alexander von Humboldt-Stiftung.

Keywords: lattice Boltzmann method | lauric acid melting | phase change material | thermal energy storage

ABSTRACT

Latent heat energy storage systems (LHESS) using phase change materials (PCMs) offer high thermal energy storage density and effective temperature regulation due to their ability to absorb and release heat at nearly constant temperatures. However, accurately simulating the melting process of PCMs remains challenging due to the nonlinear nature of heat transfer and phase transition mechanisms. In this study, the Lattice Boltzmann Method (LBM), implemented via the OpenLB framework, is employed to simulate the melting behavior of lauric acid material inside a finned rectangular cavity. The primary objective is to validate a new OpenLB numerical model against benchmark experimental data. The simulation results show excellent agreement with experimental observations in terms of liquid fraction evolution over time, particularly for the case with higher spatial and temporal resolution. Additionally, temperature measurements obtained from thermocouples at multiple locations within the cavity display the same trend in temperature evolution as observed in the numerical model, further supporting the model's reproducibility. Following validation, the model is used to study 12 additional configurations involving variations in fin aspect ratio and position. The simulations reveal that longer, thinner fins placed near the bottom of the cavity can reduce the total melting time. Between the minimum and maximum melting times obtained in this study, the fin aspect ratio and position showed a difference of 63.7%. Compared to upper fin placements, lower-position fins consistently maintained increased melting rates, with improvements ranging from 11% to 26% depending on the fin aspect ratio. In fact, higher melting rates were observed in longer and thinner fins for all positions studied, with improvements ranging from 1% to 25% depending on the position.

1 | Introduction

Latent heat energy storage systems (LHESS) are an efficient and versatile means of thermal energy storage, offering high energy density within compact volumes. These systems find application in solar energy storage, battery thermal management, electronic cooling, and building temperature regulation. Central to these systems are phase change materials (PCMs), which absorb or release thermal energy during phase transitions at a nearly constant temperature. These properties make PCM-based systems particularly advantageous for thermal management and energy storage applications. However, the low thermal conductivity of most PCMs usually requires specific strategies to enhance heat transfer. Common approaches include integrating extended surfaces, incorporating highly conductive materials (e.g., metal foams or nano-particles), or employing combinations of these techniques. Extended surfaces, such as fins, are mostly used due to their simplicity.

Numerous studies have employed the lattice Boltzmann method (LBM) to simulate heat transfer in enclosures with various fin configurations and geometries [1–3]. For example, Laouer et al. [4] demonstrated that increasing fin length and optimizing their vertical positioning significantly improved the melting performance in rectangular cavities, reducing melting time by over 70% in some configurations. Dai et al. [5] analyzed the melting process in a cavity heated from different sides using the enthalpy-based lattice Boltzmann method. The work investigated the heat transfer and flow characteristics of melting when heated from the left and bottom, showing that melting efficiency increases with Ra and that the bottom heating method surpasses the left heating method at higher Rayleigh numbers. The study also explores how the angle between the heat flux and gravity affects melting efficiency, revealing that larger angles lead to stronger natural convection and higher melting efficiency. More recently, Dai et al. [6] expanded on this analysis by looking into the thermal behavior of T-shaped fins, identifying an optimal configuration that nearly doubled the melting efficiency compared to finless systems. Meanwhile, Talati and Taghilou [7] applied the LBM to simulate PCM solidification in rectangular finned containers, validating results against analytical solutions and the finite volume method (FVM). They extended the study to a composite wall with convective boundaries, showing that embedding PCM can significantly reduce heat loss and that solidification is strongly influenced by the container material. Their results demonstrate that LBM offers reliable accuracy while being computationally more efficient than FVM. In addition, LBM has proven to be effective in modeling other advanced systems with more complex heat transfer optimization techniques, such as Mabrouk et al. [8], who studied integrated metal structures and PCM. This work demonstrated how Reynolds number, porosity, and other parameters impact thermal and energy efficiencies in porous channels embedded in PCM. These findings suggest that LBM can offer valuable insights into complex multi-phase flow scenarios in composite systems. Similarly, the use of LBM has extended to nanoparticle-enhanced phase change materials (NEPCMs), as explored by Feng et al. [9]. Their study on convection melting in a bottom-heated cavity revealed that incorporating copper nanoparticles into PCM significantly boosts heat transfer efficiency and accelerates the melting process. The LBM model effectively captured the dynamic behavior of the melting interface, showing that higher volume fractions of nanoparticles lead to faster melting and increased stored energy.

In thermal energy storage applications for industrial applications, extended surfaces such as fins represent a simple technique that can be efficiently applied to enhance the heat transfer rate within phase change material in LHESS systems. By integrating fins, the effective thermal conductivity of the system is improved as they facilitate heat distribution by increasing the contact area between the heat source and the PCM. This enhancement leads to more uniform temperature fields, accelerated phase transitions, and greater thermal efficiency. Given these advantages, researchers have extensively investigated the impact of fin geometry, positioning, and material properties on PCM melting dynamics. For example, Hosseini et al. [10] studied the melting process of PCM in a double tube heat exchanger and the effect of different fin radial lengths. The results of this study showed that employing longer fins causes a reduction in the total melting time. Ji, C. et al. [11] studied the melting process of PCM in rectangular cavities with a double horizontal fin configuration. These authors showed that short upper fins and long lower fins can reduce the PCM melting time by 40.5%. Abdi, A., Martin, V., and Chiu, J. N. W. [12] studied the PCM melting process in a rectangular cavity with vertically oriented fins on the effects of fin length and number. The authors concluded that increasing the fin length is more advantageous than increasing the number of fins. Oliveski et al. [13] studied the melting process of PCM in a rectangular cavity with fins. The results of this study show that increasing the area fraction occupied by the fin is associated with a reduction in PCM total melting time. However, the authors concluded that excessively increasing the fin volume can lead to a considerable reduction in the energy storage capacity. In addition, this study determined optimal fin aspect ratios. These examples underline the versatility of LBM in modeling various PCMs applications, although much of its potential remains underexplored, particularly in terms of optimization for industrial applications.

Although fin geometry and positioning have been extensively studied in the context of phase change materials (PCMs), most investigations rely on traditional numerical techniques such as finite volume and finite element methods. Despite providing valuable insights, these approaches are often computationally expensive and require complex meshing strategies, limiting their flexibility in handling dynamic phase interfaces. In contrast, the Lattice Boltzmann Method (LBM) offers a promising alternative, with inherent advantages for simulating complex thermal interactions and phase change processes [14, 15]. To the best of our knowledge, this is the first study to apply the Lattice Boltzmann Method to simulate the melting of lauric acid with quantitative validation against experimental data. Lauric acid, a phase change material with favorable thermophysical properties and a melting temperature close to that of human comfort, is widely used in thermal energy storage applications. Accurate numerical modeling of its phase change behavior is essential for designing efficient and reliable energy systems, making the present study an important contribution toward bridging simulation and real performance. Therefore, the specific objective of this study is to validate an LBM

TABLE 1 | Lauric acid thermal conductivity [17].

T (K)	293	303	313	323	328	333	343
κ ($Wm^{-1}K^{-1}$)	0.161	0.159	0.158	0.145	0.143	0.142	0.138

TABLE 2 | Lauric acid dynamic viscosity [17].

T (K)	321.2	322	333	344	355	372	383
μ ($kg\,m^{-1}s^{-1}$)	0.0076	0.0074	0.0054	0.0043	0.0034	0.0025	0.0021

simulation model using OpenLB [1] against experimental data from [16] for the melting of lauric acid within a rectangular cavity equipped with a horizontal fin. This validation focuses on the analysis of temperature fields, liquid fraction evolution, phase change profiles, and total melting times. Furthermore, this work seeks to evaluate the thermal performance of 12 different fin configurations, varying geometry and positioning, within the rectangular cavity to optimize heat transfer in a latent energy storage system, comparing metrics such as total melting time and temperature distribution.

2 | Problem Description

Consider an energy storage system in which thermal energy is absorbed by the lauric acid material. The latent heat of fusion is 187210 J / kg. Solid specific heat is Cps = 2180 J / kgK, and liquid specific heat is Cpl = 2390 J / kgK. The values of thermal conductivity (k) and dynamic viscosity (μ) as functions of temperature are shown in Tables 1 and 2, respectively. The thermal conductivities implemented in OpenLB, for simplification, were $\kappa_s = 0.158$ and $\kappa_l = 0.145 Wm^{-1}K^{-1}$ for the solid and liquid phases, respectively. The PCM density is 885 kg/m^3 and the thermal expansion coefficient is $0.000615 K^{-1}$ [28]. All the input parameters are summarized in Table 3.

The rectangular cavity of this study is illustrated in Figure 1. The cavity walls are all thermally insulated, except for the right-hand wall (fin included) that is heated and at a fixed temperature of T_h=70°C. The cavity height is 120 mm and its width is 50 mm. The insulated walls present a no-slip condition. The lauric acid material is initially at Tcold = 25°C, while the heated wall was at T_h = 70°C. As mentioned by Oliveski et al. [17], the lauric acid solid temperature is T*solid* = 43.5°C and the liquid temperature is T_l = 48.25°C; for simplification reasons, the melting temperature is set to T*melt* = 47.5°C in this work. As Figure 1 depicts, heat is transferred from the wall into the PCM, causing the melting of lauric acid until the whole material is in the liquid phase.

To assess the influence of fin geometry on the melting performance of the phase change material (PCM), 12 different configurations were simulated by varying the fin aspect ratio (W/E) and its vertical position (H). Three vertical positions were analyzed: H = 30, 60, and 90 mm, corresponding to lower, middle, and upper placements of the fin along the heated wall. For each position, four different fin aspect ratios were obtained by combining W = 16.67, 20, 25, 33.33 mm and E = 6, 5, 4, 3 mm. In all configurations, the PCM volume is kept constant to ensure that only the fin geometry affects the thermal behavior. The total number of cases was 12.

TABLE 3 | Input parameters for OpenLB simulation of PCM melting in a finned cavity.

Geometric parameters	
Fin width W (m)	25×10^{-3}
Fin length E (m)	4×10^{-3}
Cavity length l_x (m)	50×10^{-3}
Cavity height l_y (m)	120×10^{-3}
Simulation parameters	
Max physical time (s)	13000.0
Relaxation time τ	0.51
Resolution	100
Material properties	
Solid thermal conductivity κ_s ($W\,m^{-1}K^{-1}$)	0.158
Liquid thermal conductivity κ_l ($W\,m^{-1}K^{-1}$)	0.145
Solid specific heat $c_{p,s}$ ($J\,kg^{-1}K^{-1}$)	2180.0
Liquid specific heat $c_{p,l}$ ($J\,kg^{-1}K^{-1}$)	2390.0
Thermal expansion coefficient β (K^{-1})	6.15×10^{-4}
Dynamic viscosity μ ($kg\,m^{-1}s^{-1}$)	0.0076
Density ρ ($kg\,m^{-3}$)	885.0
Latent heat L ($J\,kg^{-1}$)	187210.0
Thermal boundary conditions	
Cold wall temperature T_c (°C)	25.0
Hot wall temperature T_h (°C)	70.0
Melting temperature T_{melt} (°C)	47.5
Physical constants	
Gravity acceleration g ($m\,s^{-2}$)	9.81

3 | Numerical Approach

For modeling the phase transition of the melting process, this work uses Gaedtke et al. [15] as a reference, and employs the double distribution thermal LBM (DDT-LBM). Firstly, we introduce

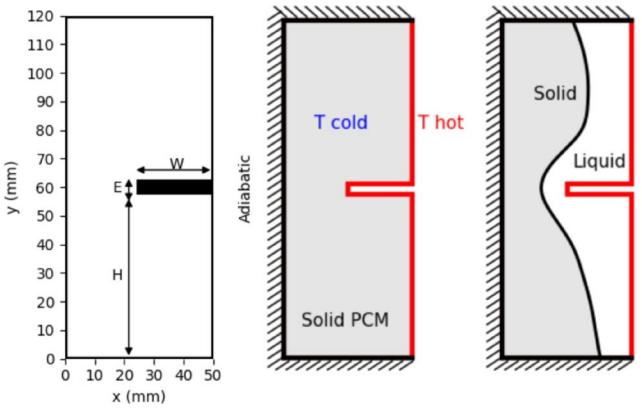

FIGURE 1 | Computational domain and problem definition schema.

some of the model equations in Section 3.1, relevant for the OpenLB implementation. The macroscopic target equations are introduced in Section 3.2. Subsequently, for numerically solving the macroscopic equations with an LB algorithm, two distribution functions g_i and f_i are introduced in Sections 3.3 and 3.4. Note that the Lattice Boltzmann Equations (LBE) are solved in their non-dimensional form. Therefore, all physical quantities are converted to lattice units prior to the simulation and reconverted before post-processing. For an overview of the dimensions of LBE, please read Krüger et al. [18].

3.1 | Model Equations

The following equations describe the key physical relationships and dimensionless numbers used in the lattice Boltzmann simulation of natural convection and phase change. These equations are derived from the simulation parameters and govern the thermophysical behavior of the system.

3.1.1 | Specific Heat and Thermal Conductivity

The effective specific heat capacity, accounting for both solid and liquid phases, is computed using the harmonic mean to represent the thermal inertia across the phase boundary.

$$c_{p,\text{ref}} = \frac{2 \cdot c_{p,s} \cdot c_{p,l}}{c_{p,s} + c_{p,l}} \tag{1}$$

where $c_{p,s} = 2180\ \text{J}/(\text{kg} \cdot \text{K})$ is the specific heat of the solid phase, and $c_{p,l} = 2390\ \text{J}/(\text{kg} \cdot \text{K})$ is the specific heat of the liquid phase.

Likewise, the effective thermal conductivity for the phase-change material, considering both solid and liquid phases, is calculated using the harmonic mean to account for the interface between phases, described as

$$\kappa_{\text{ref}} = \frac{2 \cdot \kappa_s \cdot \kappa_l}{\kappa_s + \kappa_l} \tag{2}$$

where $\kappa_s = 0.158\ \text{W}/(\text{m} \cdot \text{K})$ is the thermal conductivity of the solid phase, and $\kappa_l = 0.145\ \text{W}/(\text{m} \cdot \text{K})$ is the thermal conductivity of the liquid phase.

It is important to note that the thermal conductivity of the phase change material (PCM) during the melting process is modeled using a fixed effective value, calculated as the harmonic mean of the solid and liquid phase conductivities ($\kappa_s, \kappa_l, \kappa_{\text{ref}}$). This simplification accounts for the transition between phases while acknowledging that thermal conductivity can vary spatially and temporally during melting due to the evolving solid–liquid interface. The use of a fixed value is justified by the small 8.2% difference between the solid and liquid conductivities and by validation results, which showed adequate agreement with experimental data, indicating that dynamic variations had a negligible impact on the liquid fraction results.

To characterize the ratio of thermal conductivity between the solid and liquid phases, the ratio of thermal conductivities was defined as

$$R_\kappa = \frac{\kappa_s}{\kappa_l} \tag{3}$$

This ratio is used to adjust the thermal properties during the phase transition in the simulation.

3.1.2 | Thermal Diffusivity

Thermal diffusivity, which quantifies the rate of heat diffusion relative to thermal inertia, is defined as:

$$\alpha = \frac{\kappa_{\text{ref}}}{\rho \cdot c_{p,\text{ref}}} \tag{4}$$

where $\rho = 885\ \text{kg}/\text{m}^3$ is the density, κ_{ref} is the effective thermal conductivity, and $c_{p,\text{ref}}$ is the effective specific heat.

3.1.3 | Kinematic Viscosity

Kinematic viscosity, representing the ratio of dynamic viscosity to density, is given by:

$$\nu = \frac{\mu}{\rho} \tag{5}$$

where $\mu = 7.6 \times 10^{-3}\ \text{kg}/(\text{m} \cdot \text{s})$ is the dynamic viscosity, and $\rho = 885\ \text{kg}/\text{m}^3$ is the density.

3.1.4 | Prandtl Number

The Prandtl number, representing the ratio of momentum diffusivity to thermal diffusivity, is defined as:

$$\text{Pr} = \frac{\nu}{\alpha} \tag{6}$$

3.1.5 | Rayleigh Number

The characteristic length for the rectangular cavity with an embedded fin is defined as the hydraulic diameter, calculated as four times the area of the phase-change material divided by the perimeter, including the fin boundaries:

$$L_{\text{char}} = \frac{4 \times \text{Area}}{\text{Perimeter}} = \frac{4 \cdot \left(l_x \cdot l_y - \text{E} \cdot \text{W}\right)}{\left(l_x + l_x + l_y + l_y + W + W\right)} \tag{7}$$

where $l_x = 0.05$ m is the cavity length, $l_y = 0.12$ m is the cavity height, $\text{W} = 0.025$ m is the fin length, and $\text{E} = 0.004$ m is the fin height. As a consequence, the Rayleigh number, which quantifies the strength of buoyancy-driven convection relative to viscous and thermal diffusion, is expressed as:

$$\text{Ra} = \frac{g \cdot \beta \cdot \left(T_{\text{h}} - T_{\text{m}}\right) \cdot L_{\text{char}}^3}{\alpha \cdot \nu} \tag{8}$$

where $g = 9.81\ \text{m}/\text{s}^2$ is the gravitational acceleration, $\beta = 6.15 \times 10^{-4}\ \text{K}^{-1}$ is the thermal expansion coefficient, $T_{\text{h}} = 70.0^{\circ}\text{C}$ is the hot wall temperature, $T_{\text{m}} = 47.5^{\circ}\text{C}$ is the melting temperature, L_{char} is the characteristic length, α is the thermal diffusivity, and ν is the kinematic viscosity.

Please, note that in applications with high temperature differences, or low viscosity or thermal diffusivity, causing high Rayleigh number (Ra) flows, numerical diffusion can significantly undermine simulation accuracy. The numerical diffusion artifact can potentially smooth temperature and velocity gradients, distorting flow features like boundary layers and convective cells. To mitigate these effects and improve fidelity, finer grids or higher-order numerical schemes are recommended.

3.2 | Macroscopic Equations

The fluid is considered weakly compressible, described by the Navier–Stokes equation (NSE) and the Advection–diffusion equation (ADE) for the enthalpy H as follows

$$\frac{\partial \rho}{\partial t} + \nabla \cdot (\rho \boldsymbol{u}) = 0 \tag{9}$$

$$\frac{\partial (\rho \boldsymbol{u})}{\partial t} + \nabla \cdot (\rho \boldsymbol{u}\boldsymbol{u}) = -\nabla p + \nabla \cdot (\nu \nabla \boldsymbol{u}) + \boldsymbol{F} \tag{10}$$

$$\frac{\partial (\rho H)}{\partial t} = -\nabla \cdot \left(\rho c_p T \boldsymbol{u}\right) + \nabla \cdot (\lambda \nabla T) \tag{11}$$

where t denotes time and ρ, $\boldsymbol{u}$, p, c_p and T are the fluid's density, velocity, pressure, specific heat at constant pressure, and temperature, respectively. The dynamic viscosity and thermal conductivity are given by ν and λ. The buoyancy force $\boldsymbol{F}$ is calculated by the Boussinesq approximation with

$$\boldsymbol{F} = \rho \beta \boldsymbol{g}\left(T - T_{\text{ref}}\right) \tag{12}$$

where T_{ref} is the reference temperature, β is the thermal expansion coefficient, and $\boldsymbol{g}$ is the gravitational vector. For the enthalpy,

$$H = c_p T + f_l L \tag{13}$$

is described as a function of the liquid fraction (f_l), the latent heat (L), the temperature, and the specific heat.

3.3 | Lattice Boltzmann Method for the Enthalpy Equation

To numerically solve Equation (11), this implementation follows the LBM proposed by Huang et al. [19, 20] for which the particle distribution function g_i is

$$g_i\left(\boldsymbol{x} + c_i \Delta t, t + \Delta t\right) = g_i(\boldsymbol{x}, t) - \frac{\Delta t}{\tau_g}\left(g_i(\boldsymbol{x}, t) - g_i^{eq}(\boldsymbol{x}, t)\right) \tag{14}$$

where i is the discrete direction, $\boldsymbol{c_i}$ the discrete velocity in direction i, and the relaxation time $\tau_g = \frac{\alpha}{c_s^2} + \frac{1}{2}\Delta t$ is a function of thermal diffusivity $\alpha = \frac{\lambda}{\rho_0 c_{p,ref}}$. The equilibrium distribution function is given by

$$g_i^{eq} = \begin{cases} H - c_{p,\text{ref}} T + \omega_i c_p T\left(\dfrac{c_{p,\text{ref}}}{c_p} - \dfrac{\mathbf{u}\cdot\mathbf{u}}{2c_s^2}\right), & i = 0 \\ \omega_i c_p T\left(\dfrac{c_{p,\text{ref}}}{c_p} + \dfrac{\mathbf{u}\cdot\mathbf{c}_i}{c_s^2} + \dfrac{\left(\mathbf{u}\cdot\mathbf{c}_i\right)^2}{2c_s^4} - \dfrac{\mathbf{u}\cdot\mathbf{u}}{2c_s^2}\right), & i \neq 0 \end{cases} \tag{15}$$

The discrete weights ω_1, the discrete velocities c_i and the speed of sound c_s are given by the standard D2Q5 velocity set [18]. As a consequence, the enthalpy is then calculated from the zeroth moment of g_i with

$$H = \sum_i g_i(\boldsymbol{x}, t) \tag{16}$$

From that, the temperature T and liquid fraction f_l are obtained by

$$T = \begin{cases} T_s - \dfrac{H_s - H}{c_{p,s}} & H < H_s \\ \dfrac{H_l - H}{H_l - H_s} T_s + \dfrac{H - H_s}{H_l - H_s} T_l & H_s \leq H \leq H_l \\ T_l + \dfrac{H - H_l}{C_{p,l}} & H > H_l \end{cases} \tag{17}$$

$$f_l = \begin{cases} 0 & H < H_s \\ \dfrac{H - H_s}{H_l - H_s} & H_s \leq H \leq H_l \\ 1 & H > H_l \end{cases} \tag{18}$$

The enthalpy at solid temperature (T_s) and liquid temperature (T_1) are given by H_s and H_l. For the sake of numerical stability [20] the reference specific heat is defined as

$$\lambda = \left(1 - f_l\right)\lambda_s + f_l \lambda_1 \tag{19}$$

$$c_p = \left(1 - f_l\right)c_{p,s} + f_1 c_{p,l} \tag{20}$$

$$c_{p,\text{ref}} = \frac{2 c_{p,s} c_{p,l}}{c_{p,s} + c_{p,l}} \tag{21}$$

Following the methodology proposed by Gaedtke et al. [15], a two relaxation times (TRT) collision operator is implemented so as to limit the numerical diffusion across the phase change

interface. The particle distribution function in the case of TRT collision is:

$$g_i\left(\mathbf{x}+\mathbf{c}_i\Delta t, t+\Delta t\right)=g_i(\mathbf{x},t)-\frac{\Delta t}{\tau_g^+}\left(g_i^+(\mathbf{x},t)-g_i^{\mathrm{eq}+}(\mathbf{x},t)\right) -\frac{\Delta t}{\tau_g^-}\left(g_i^-(\mathbf{x},t)-g_i^{\mathrm{eq}-}\mathbf{x},t)\right) \tag{22}$$

with

$$g_i^+=\frac{1}{2}\left(g_i+g_i\right) \tag{23}$$

$$g_i^-=\frac{1}{2}\left(g_i-g_i\right) \tag{24}$$

$$g_i^{\mathrm{eq}+}=\frac{1}{2}\left(g_i^{\mathrm{eq}}+g_i^{\mathrm{eq}}\right) \tag{25}$$

$$g_i^{\mathrm{eq}-}=\frac{1}{2}\left(g_i^{\mathrm{eq}}-g_i^{\mathrm{eq}}\right) \tag{26}$$

The two relaxation times are given by

$$\tau_g^-=\frac{\alpha}{c_s^2}+\frac{\Delta t}{2} \tag{27}$$

$$\Lambda=\left(\frac{\tau_g^+}{\Delta t}-\frac{1}{2}\right)\left(\frac{\tau_g^-}{\Delta t}-\frac{1}{2}\right) \tag{28}$$

where the parameter $\Lambda=\frac{1}{4}$ is found to limit the numerical diffusion across the interface [15, 21].

3.4 | Lattice Boltzmann Method for the Fluid Flow

In this work, using the same methodology as Gaedtke et al. [15], the partially saturated method (PSM) proposed by Noble and Torczynski [22] is implemented to compute the phase interface location evolution. Therefore, the particle distribution function f_i is described as

$$f_i\left(\mathbf{x}+\mathbf{c}_i\Delta t, t+\Delta t\right)=f_i(\mathbf{x},t)+B\Omega_i^s(\mathbf{x},t)+(1-B)\Omega_i^f(\mathbf{x},t)+F_i \tag{29}$$

with the weighting function $B(\boldsymbol{x},t)$

$$B(\mathbf{x},t)=\frac{\left(1-f_l(\mathbf{x},t)\right)\left(\frac{\tau_f}{\Delta t}-\frac{1}{2}\right)}{f_I(\mathbf{x},t)+\left(\frac{\tau_f}{\Delta t}-\frac{1}{2}\right)} \tag{30}$$

The solid collision operator $\Omega_i^s(\boldsymbol{x},t)$ is

$$\Omega_i^s(\mathbf{x},t)=\left(f_i^{eq}\left(\rho,\mathbf{u}_s\right)-f_i(\mathbf{x},t)\right)+\left(1-\frac{\Delta t}{\tau_f}\right)\left(f_i(\mathbf{x},t)-f_i^{eq}(\rho,\mathbf{u})\right) \tag{31}$$

with solid velocity $u_s=0$. The fluid collision operator $\Omega_i^f(\boldsymbol{x},t)$ is

$$\Omega_i^f(\mathbf{x},t)=\frac{\Delta t}{\tau_f}\left(f_i^{eq}\left(\rho_f,\mathbf{u}\right)-f_i(\mathbf{x},t)\right) \tag{32}$$

The equilibrium distribution function f_i^{eq} is described as

$$f_i^{eq}=\omega_i\rho\left(1+\frac{\mathbf{u}\cdot\mathbf{c_i}}{c_s^2}+\frac{\left(\mathbf{u}\cdot\mathbf{c_i}\right)^2}{2c_s^4}-\frac{\mathbf{u}\cdot\mathbf{u}}{2c_s^2}\right) \tag{33}$$

and the relaxation time τ_f is calculated from

$$\tau_f=\frac{\nu}{c_s^2}+\frac{1}{2}\Delta t \tag{34}$$

The weights ω_i, the discrete velocities $\boldsymbol{c_i}$ and the speed of sound c_s are calculated using the standard D2Q9 velocity set for the 2D simulation ([18]). The fluid's density ρ, pressure p, and fluid velocity u are then calculated from

$$\rho(\boldsymbol{x},t)=\frac{p}{c_s^2}=\sum_i f_i(\boldsymbol{x},t) \tag{35}$$

$$\boldsymbol{u}(\boldsymbol{x},t)=\frac{1}{\rho}\sum_i c_i f_i(x,t) \tag{36}$$

Simulating phase change processes poses significant challenges in terms of numerical stability due to the abrupt variation in physical properties between the two phases. To mitigate these issues, various stabilization methods can be employed. In this work, the Smagorinsky LBM model [23] is applied. Although originally developed for turbulence simulations, its applicability in stabilizing flow simulations with small relaxation times has also been demonstrated [24]. We therefore apply this model to stabilize the laminar multiphase flow in situations involving low relaxation times.

In this approach, the viscosity ν in (34) is replaced by an effective viscosity $\nu_{\mathrm{eff}}=c_s^2\left(\tau_{eff}-0.5\Delta t\right)$, which consists of the molecular viscosity ν and the eddy viscosity ν_t given by

$$\nu_{eff}=\nu+\nu_t=\nu+\left(C_S\Delta\right)^2\sqrt{2\sum_{\alpha\beta}S_{\alpha\beta}S_{\alpha\beta}} \tag{37}$$

The Smagorinsky constant is $C_S=0.1$ and Δ is the filter width, which is set equal to Δx. The strain rate $S_{\alpha,\beta}$ is computed from the non-equilibrium part of the distribution function:

$$S_{\alpha\beta}=-\frac{1}{2\rho\tau_{eff}c_s^2}\sum_i c_{i\alpha}c_{i\beta}\left(f_i-f_i^{eq}\right) \tag{38}$$

Finally, the strain rate from (38) is substituted in (37) to obtain an expression for τ_{eff}, which is then used in the collision operator (31).

3.5 | Validation With an Experimental Setting

For the implementation of the numerical approach described in Sections 3.1, 3.2, and 3.3, the OpenLB framework was used, an open-source tool based on the Lattice Boltzmann Method (LBM).

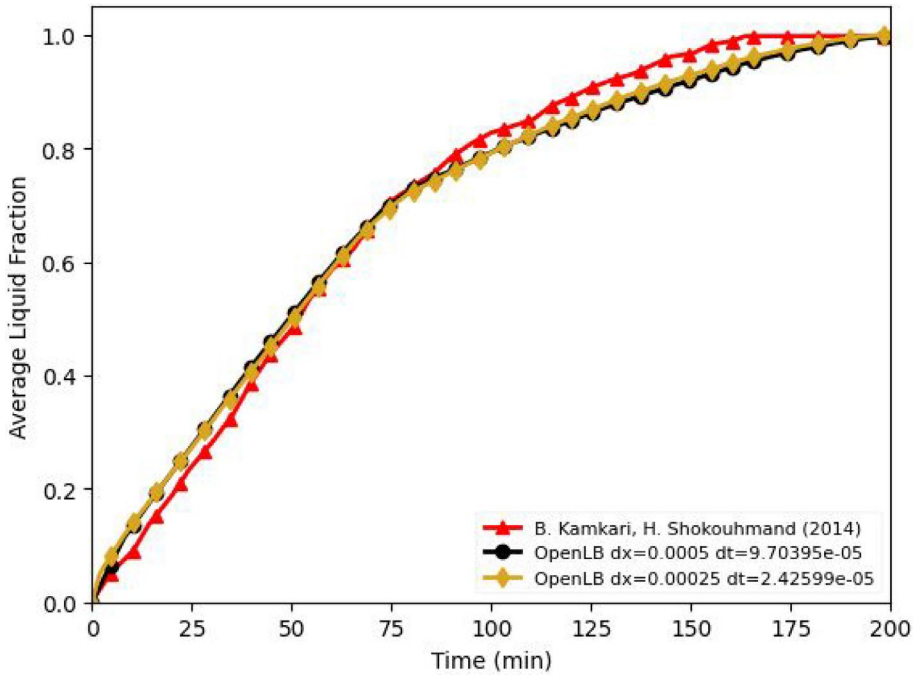

FIGURE 2 | Average liquid fraction versus time: Experimental and OpenLB results.

The detailed numerical configuration was applied within this environment, allowing the simulation of thermal and phase change phenomena. The results were visualized using ParaView and PyVista. The results from OpenLB were validated against the experimental results of Kamkari and Shokouhmand [16]. The authors investigated the melting process of lauric acid in a vertical rectangular cavity, 50 mm wide, 120 mm high, and 120 mm deep. Validation was performed quantitatively through average liquid fraction analysis and qualitatively through liquid fraction profile analysis.

The liquid fraction progress over time is shown in Figure 2, with numerical results from the present study compared to experimental results from Kamkari and Shokouhmand [16]. In Figure 2, the black curve represents the numerical case referred to as N100, which corresponds to a spatial resolution of $dx = 0.0005$ m and time step $dt = 9.70395 \times 10^{-5}$ s. The yellow curve corresponds to the N200 case, which uses a finer resolution of dx = 0.00025 and $dt = 2.42599 \times 10^{-5}$. The numerical models were evaluated by calculating the L_2 errors and L_∞ errors.

$$L_2 = \sqrt{\frac{1}{n}\sum_{i=1}^{n}\left(y_i - \hat{y}_i\right)^2} \tag{39}$$

$$L_\infty = \max_{i=1,\ldots,n} | y_i - \hat{y}_i | \tag{40}$$

The results are presented in Table 4. As results in Table 4 show, N200 is more performant. With smaller errors in both norms, the N200 case presents relatively low overall error and deviation. Quantitatively, N200 is an acceptable simulation case based on its superior accuracy and consistency compared to both the experimental data ([16]) and the N100 dataset. The L_2 error between N200 and the experimental data is smaller (0.029087) than that of N100 (0.032375), indicating that N200 has a closer overall alignment with the experimental results. The L_∞ error for N200 (0.049406) is also lower than for N100 (0.052387), demonstrating that N200 avoids significant outliers or extreme deviations. Furthermore, the small errors between N100 and N200 ($L_2 = 0.006303$, $L_\infty = 0.016855$) show that N200 maintains consistency with N100 while achieving improved fidelity to the experimental data.

TABLE 4 | Comparison of Errors ($L2$-norm, and $L\infty$-norm) between Experimental, N100, and N200.

Comparison	L_2	L_∞
Kamkari and Shokouhmand [16] versus N100	0.032375	0.052387
Kamkari and Shokouhmand [16] versus N200	0.029087	0.049406
N100 versus N200—OpenLB	0.006303	0.016855

The validation of the N200 simulation case can be further detailed by analyzing the comparison between the numerical temperature fields (top row) and the experimental photographs (bottom row) shown in Figure 3. These images depict the temperature distribution and phase change evolution at different time intervals ($t = 10$ min, $t = 20$ min, $t = 30$ min, $t = 40$ min, and $t = 50$ min). The experimental images were obtained using special lighting photography, as described in [16], which enabled the clear visualization of the phase change interface. White regions correspond to solid PCM and black regions to liquid PCM. Initially, the authors observed that the liquid layer forms uniformly along the heated right wall, indicating conduction-dominated heat transfer. Over time, buoyancy-driven convection causes the melted region to expand more rapidly in the upper part of the cavity, establishing a circulating current.

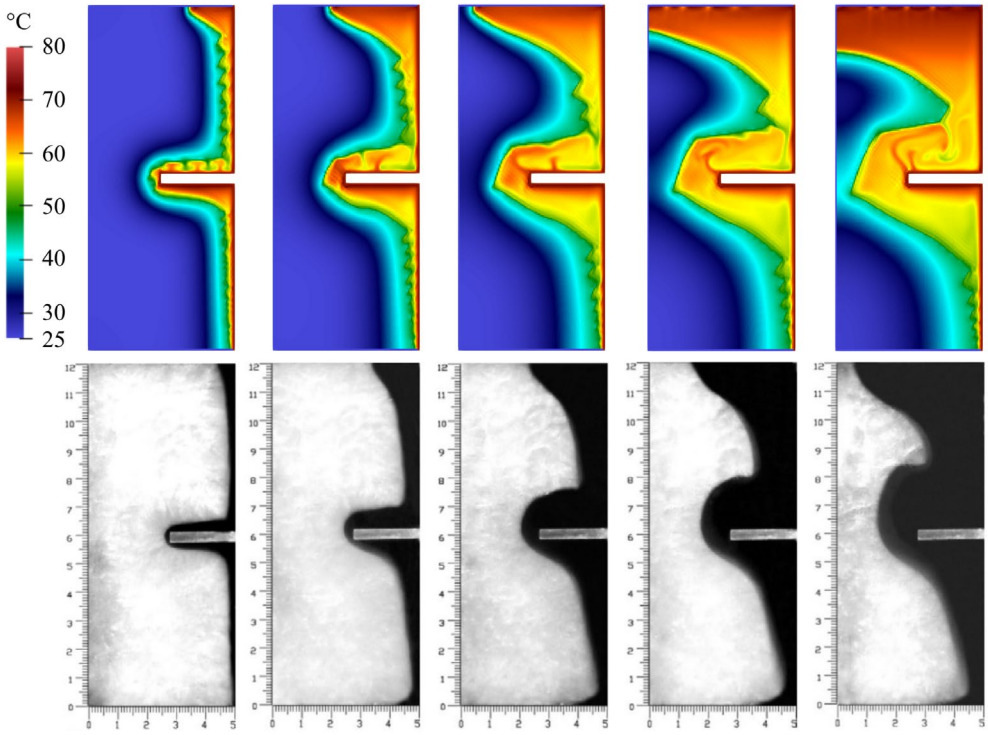

FIGURE 3 | OpenLB Numerical temperature fields vs. Experiment photographs from Kamkari and Shokouhmand [16]: (a) t = 10 min; (b) t = 20 min; (c) t = 30 min; (d) t = 40 min; (e) t = 50 min.

These flow characteristics gradually diminish as the solid PCM volume decreases. At early times ($t = 10$ min and $t = 20$ min), the thermal penetration is primarily confined to the regions near the heated fin. The simulation accurately reproduces the sharp thermal gradient observed in the experiments. As time progresses ($t = 30$ min, $t = 40$ min, and $t = 50$ min), the temperature field becomes more diffuse, and the melting front advances deeper into the cavity. The simulation results display continuous temperature gradients with precise boundary layer definitions, showing the dominant conduction and convection areas. In contrast, the experimental photographs have a grainier appearance due to the imaging process, with less sharply defined boundaries between the melted and unmelted regions. While the overall shape and progression of the melting front are similar in both the simulation and the experiment, subtle differences can be observed. The experimental results show a smoother melting zone but not much detail in terms of fluid flow. The numerical results show more details on the fluid flow, although the melting front appears too sharply defined, depending on the reference used.

In the simulation, the wall temperature (Twall) is fixed to replicate the experimental setup, ensuring a consistent thermal boundary condition at the heated fin. The remaining walls are modeled with a bounce-back condition, representing thermal insulation, which aligns with the experimental configuration. Because Twall is fixed, the temperature difference between the heated wall and the PCM decreases over time as the material warms and melts. As a consequence, the heat transfer coefficient decreases through time as well, leading to a reduction in the heat transfer rate from the wall to the PCM. As evidence to that effect, one can observe a proportional deceleration of the melting process toward the end of the melting, which is evident in both the simulation and experimental results. If a constant heat flux condition were applied instead of a fixed temperature, the heat transfer rate would remain steady, potentially mitigating the decrease in heat transfer coefficient over time as the phase change interface evolves. As a consequence, the full melting process of lauric acid in the latent heat energy storage system (LHESS) could occur in a shorter time, as the sustained energy input would accelerate the phase transition and reduce the time required for complete melting.

In that context, the simulation accurately reproduces this thermal and phase-change evolution under the specified conditions. At early times (t = 10 min and t = 20 min), the thermal penetration is primarily observed near the heated fin, with sharp thermal gradients that match the experimental observations. As time progresses (t = 30 min, t = 40 min, and t = 50 min), the simulation shows a further evolved melting interface and more diffuse temperature distribution, mimicking the convective behavior seen in the experiment. The numerical fields also provide detailed boundary layer definitions, distinguishing conduction-dominated and convection-dominated regions. While the overall shape and progression of the melting front are in strong agreement between simulation and experiment, visual differences emerge due to the nature of the representations: the experimental images show smoother transitions between phases, whereas the simulation captures more detailed gradients and flow structures. This comparison highlights the complementary nature of numerical and experimental approaches in understanding phase change behavior in LHESS.

In Figure 4, velocity vectors are illustrated at t = 10 min. In the cavity's upper area, the flow is characterized by a vertical upward motion near the heated right wall, driven by buoyancy forces, forming a boundary layer that extends toward the top of the cavity, which is thermally insulated. This motion transitions into a horizontal spread at the top, creating a single recirculation zone in the upper-left corner of the liquid material. In contrast, the introduction of the heated fin (Figure 4) significantly alters the flow dynamics, generating secondary recirculation zones both above and below the fin. These swirling patterns enhance mixing and redistribute the flow within the cavity, creating localized high-velocity regions near the fin. The deflection caused by the fin results in a more complex flow structure, with increased velocity magnitudes compared to the simpler, more laminar flow in the finless case. This demonstrates the fin's effectiveness in promoting convective mixing and enhancing heat transfer within the cavity. One can notice sharp edges in the phase change zone; however, the overall result of the numerical simulations is a close replication of the experimental temperature patterns across the time intervals. Key thermal features, such as the thermal boundary layer around the heated fin and the propagation of the melting front, are captured well. The results are also in conformity with Oliveski et al. [17]. Figure 5 presents a comparison between experimental temperature data obtained from thermocouples [16] (Figure 5a) and numerical results from OpenLB simulations (Figure 5b) at various spatial locations within the system. The simulation results show strong agreement with the experimental data, accurately capturing the overall temperature evolution, the shape of the heating curves, and the relative behavior across different thermocouple positions. Notably, the characteristic melting plateau—indicating the phase change process—is well reproduced in the simulation, particularly at locations like T3 and T5, where the temperature rise slows down due to latent heat absorption. Additionally, the time each thermocouple reaches the melting temperature is closely matched, reflecting the correct propagation of the thermal front. Final temperature values and the relative ordering of the curves are consistent between the experimental and numerical results, demonstrating that OpenLB reliably models both heat transfer and phase change behavior in the system.

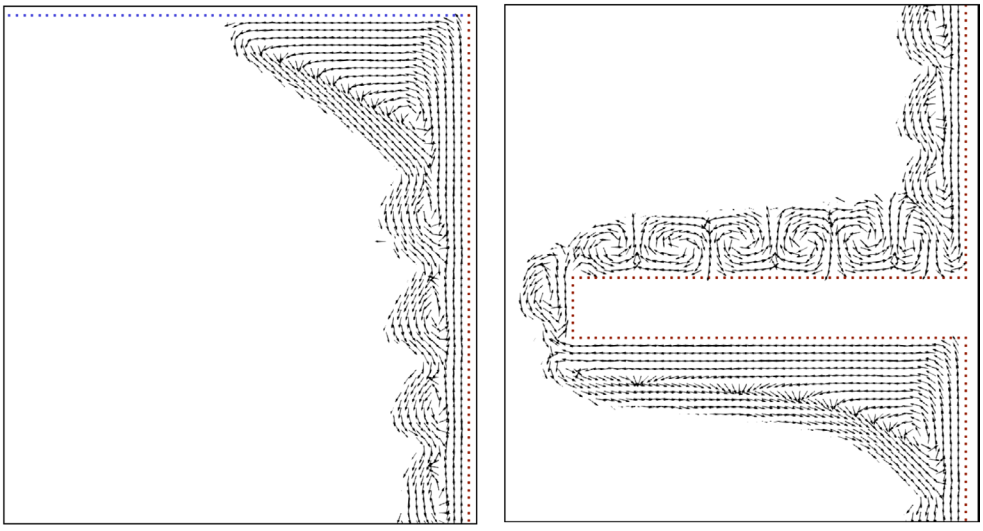

FIGURE 4 | Velocity fields at t = 10 min: (a) upper right area; (b) fin area.

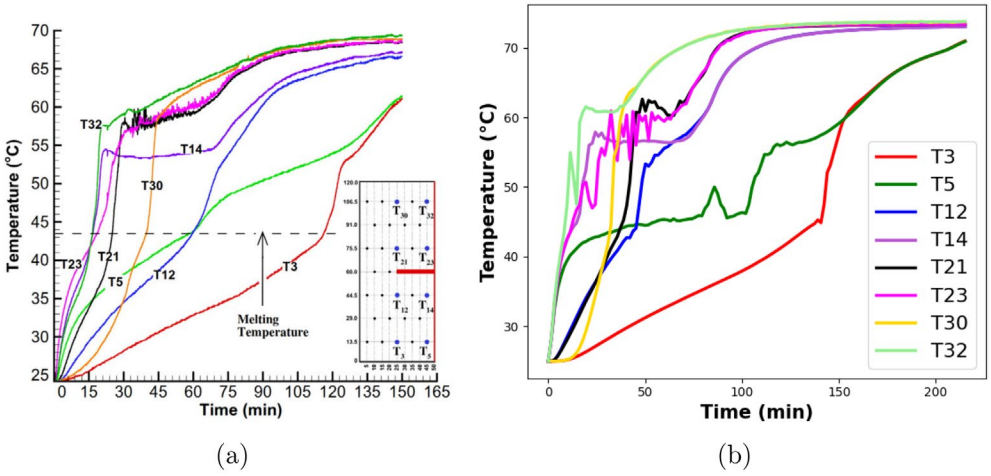

FIGURE 5 | Temperature evolution at Tn location: (a) Experimental results from [16]; (b) OpenLB results.

4 | Experiments and Results

This work investigates the influence of fin geometry and positioning on the melting behavior of a phase change material within a rectangular cavity. Numerical simulations are conducted to analyze transient liquid and solid fraction fields, velocity distributions, and temperature contours. Key performance metrics, such as the average liquid fraction over time and temperature evolution at specific locations, are evaluated to provide insights into heat transfer mechanisms and phase change efficiency.

An animation illustrating the melting process of lauric acid is available in Video S1 for the qualitative analysis. The video depicts the liquid and solid fraction fields, velocity vectors, and temperature contours. Subsequent sections will analyze the influence of fin aspect ratios, positions, and thermal distributions on PCM behavior to inform the optimization of energy storage system designs.

4.1 | Influence of Fin Aspect Ratio (W / E)

The intensity of fluid flow, as depicted in Figure 6, plays an important role in heat transfer and the overall phase change process. Regions characterized by pronounced fluid flow promote convective heat transfer within the material and accelerate phase change. The fin dimensions, denoted by W and E, significantly influence flow behavior. While maintaining a constant fin cross-sectional area, altering the fin aspect ratio yields results indicating that thin, elongated fins obstruct and redirect the fluid flow. This suggests increased localized fluid movement and enhanced heat transfer efficiency in the vicinity of the fin.

Figure 7 demonstrates the liquid fraction as a function of time, confirming the direct relationship between phase change rates and heat transfer. Systems exhibiting more intense fluid flow demonstrate accelerated melting, as evidenced by the steeper initial slopes of the melting curves. At any given time, higher liquid fraction values correlate with enhanced convective heat transfer, which is facilitated by optimized fin dimensions or aspect ratios. For example, configurations with larger aspect ratios ($AR = W / E$) typically initially exhibit faster melting due to the increase in heat transfer area relative to the volume of the fluid.

It is evident that a more intense fluid flow, as illustrated in Figure 6, directly results in stronger convective heat transfer and a more rapid phase change, as observed in Figure 7. Larger aspect ratios enhance heat exchange efficiency, particularly during the initial stages of melting. However, as cavity height increases (e.g., $H = 90\text{mm}$), the influence of the aspect ratio diminishes. This suggests a transition from a convection-dominated to a conduction-dominated heat transfer regime, wherein the significance of flow intensity decreases over time. Thinner and longer fins intensify localized flow, thus improving initial melting rates. Conversely, narrower and shorter fins lead to weaker convection, slower heat transfer, and reduced phase change rates.

These insights underscore the importance of optimizing fin dimensions and cavity aspect ratios to achieve more efficient phase change performance. The interplay between fin geometry and fluid flow intensity significantly influences heat transfer and phase change behavior. Optimizing these parameters can enhance the efficiency of latent heat storage systems, particularly during the initial stages where natural convection is dominant. As cavity height increases, conduction gradually becomes the primary mode of heat transfer, thus highlighting the need for tailored designs based on specific thermal requirements.

4.2 | Influence of Fin Position (H)

The fin's placement significantly influences fluid flow patterns, heat transfer, and phase change rates, as illustrated in Figure 8.

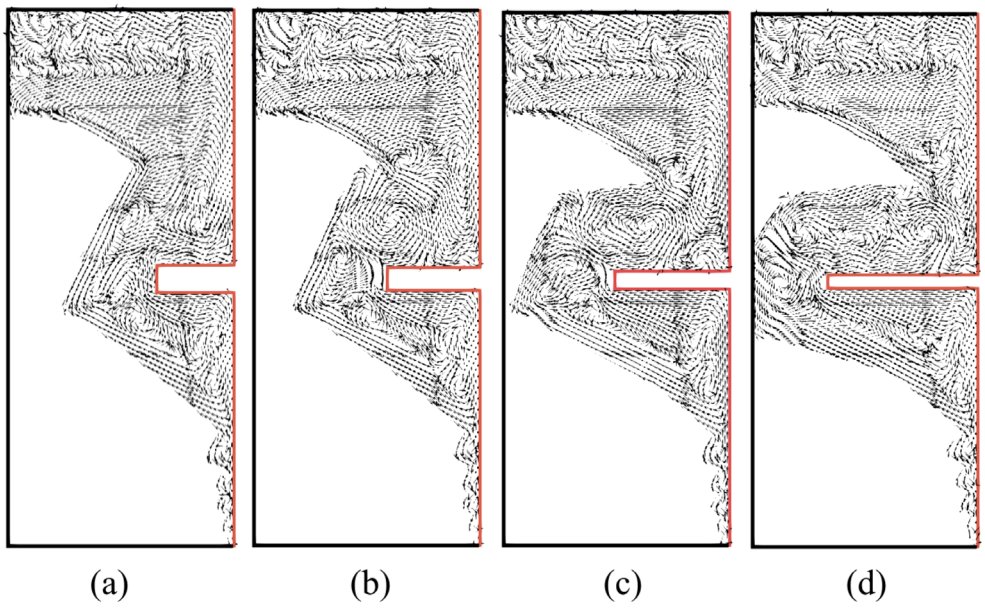

FIGURE 6 | Velocity fields at t = 60 min in different fin dimensions.

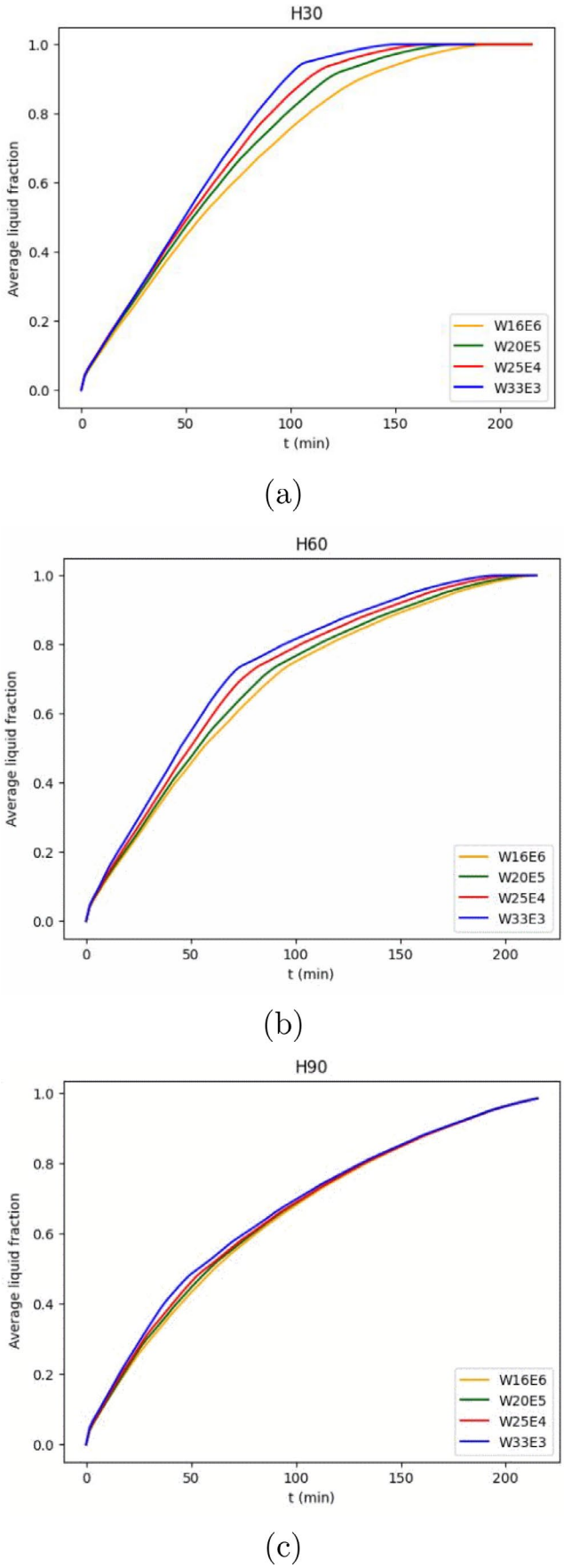

FIGURE 7 | Average liquid fraction vs. Time with different fin dimensions: (a) fin in lower position (H30), (b) fin in middle position (H60), (c) fin in upper position (H90).

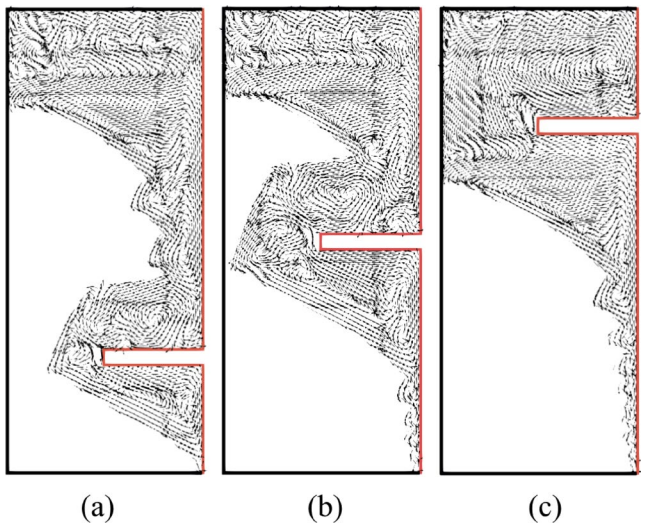

FIGURE 8 | Velocity fields at t = 60 min for different fin positions (H).

The three analyzed configurations—shown in Figure 8a–c—represent fin positions near the bottom, middle, and top of the cavity, respectively. Each configuration uniquely alters the flow behavior and thermal performance.

Figure 9 highlights the impact of fin position on the average liquid fraction over time. The results demonstrate that configuration (a), corresponding to the lower fin placement, achieves the fastest phase change rate due to the overall increase in heat transfer across the cavity. Configuration (c) exhibits slower melting rates due to the limited heat transfer to the solid material that accumulates in the lower regions of the cavity.

4.3 | Comparative Analysis

Figure 10 displays the melting total time (in minutes) for all the different configurations. Different cavities show total melting times ranging from a minimum of 129.4 min (H30W33E3) to a maximum of 211.8 min (H90W16E6). The difference of 63.7% represents an improvement to the heat transfer process. It means that the full melting process happened much faster in H30W33E3, even though the energy storage capacity was maintained the same (PCM volume). Therefore, building a longer and thinner fin in the lower area of the cavity proved to be an efficient workaround to the low thermal conductivity limitation of lauric acid. We understand that the effectiveness of the specific installation was due to the increased localized heat transfer coefficients in the surrounding area of the fin, creating greater exposure of the heat source to the solid PCM.

Generally speaking, for applications in which thermal charging is required, results show that melting rates are higher with long and thin fins placed in areas where PCM naturally gets deposited. Conversely, fins positioned farther away, as H90W16E6 from the solid material may still provide an augmented contact area for increased heat flux; but they are less effective and not recommended for applications requiring complete PCM melting

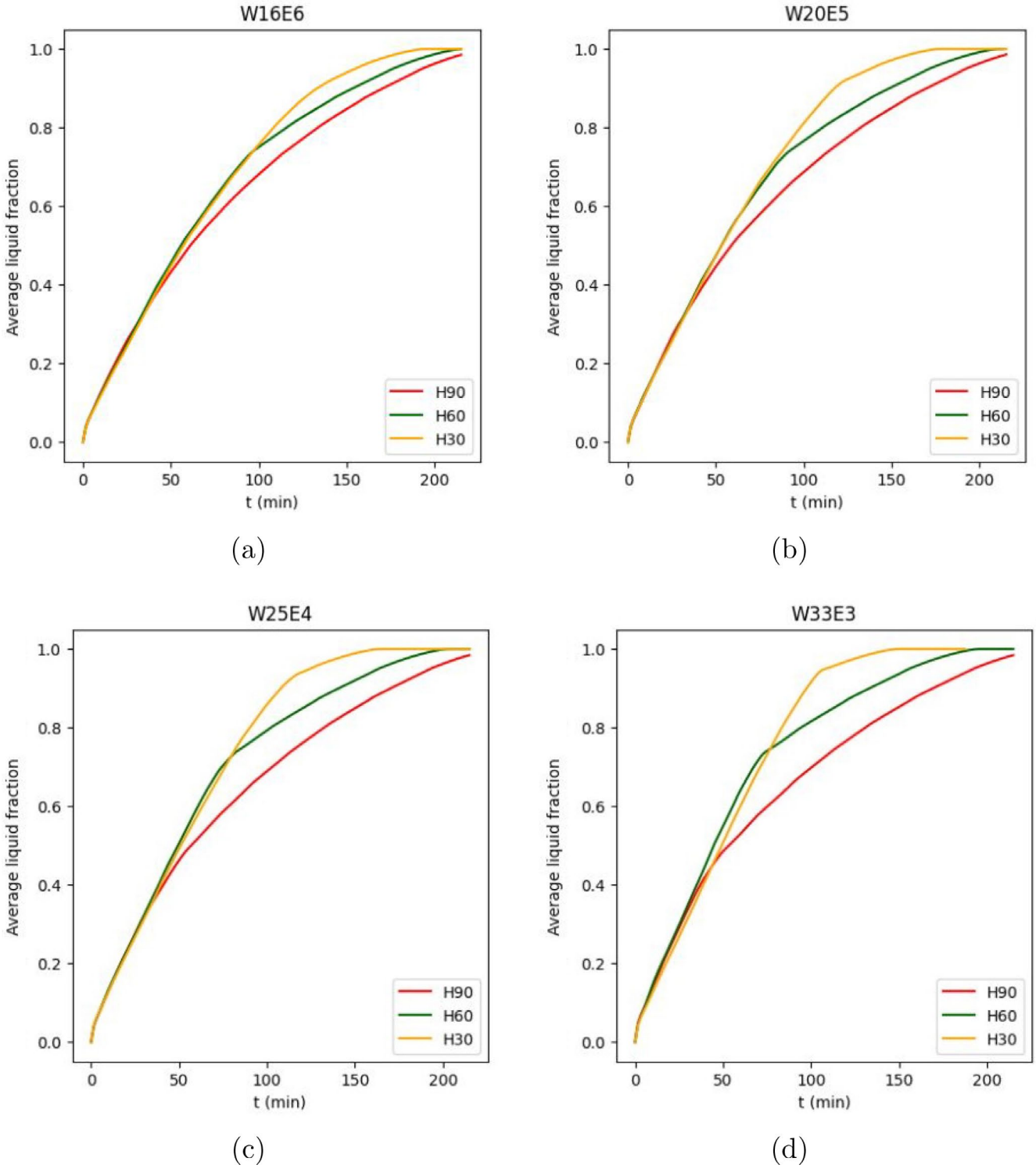

FIGURE 9 | Average liquid fraction versus Time in different fin positions: (a) W16E6, (b) W20E5, (c) W25E4, (d) W33E3.

in short timeframes, due to reduced proximity to the heat source and slower thermal penetration.

4.4 | Temperature Distribution at Specific Locations

The temperature evolution obtained from the numerical simulations provides detailed insights into the thermal and flow characteristics of the PCM during melting within enclosures. Consistent with experimental observations, the temperature measurements shown in Figure 11 (T3, T5, T12, T14, T21, T23, T30, and T32) offer detailed information on the thermal and flow behavior of the PCM during melting. Figure 12 illustrates the temperature evolution at these respective points. In all cases, when the numerically modeled temperature is below the melting point, heat is transferred to the solid PCM via conduction. The simulations reveal increased heat transfer rates near the

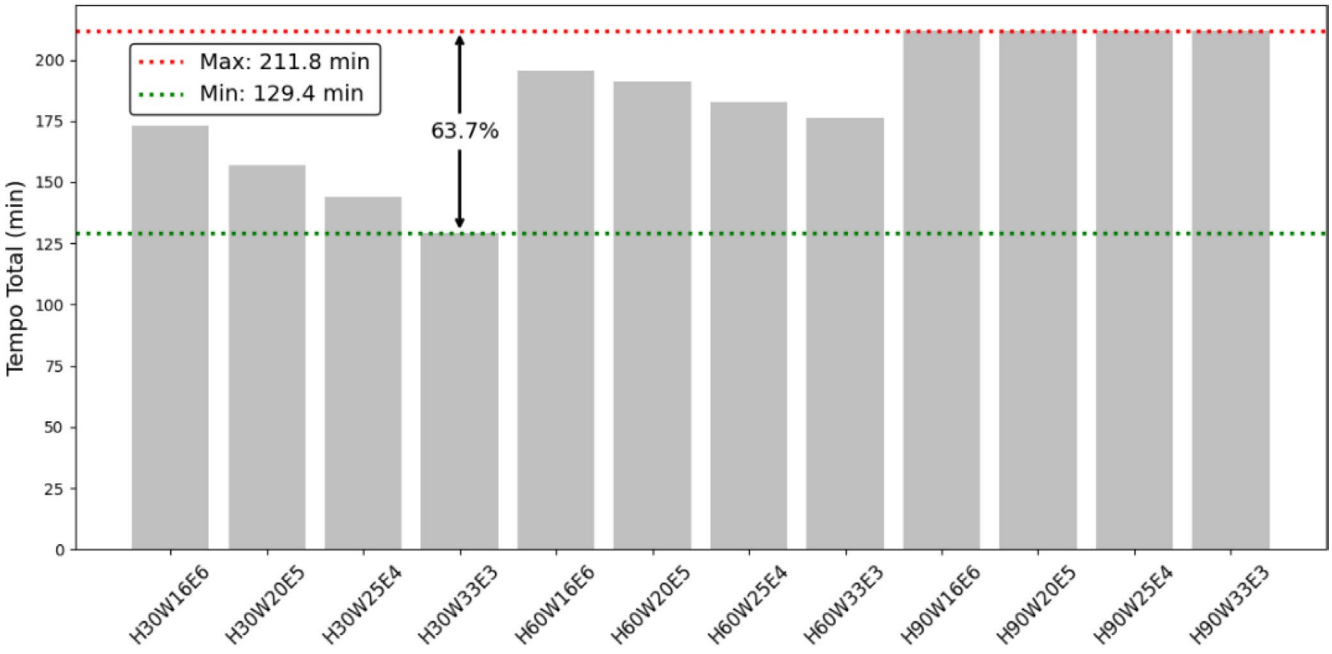

FIGURE 10 | Total melting times for all cases studied.

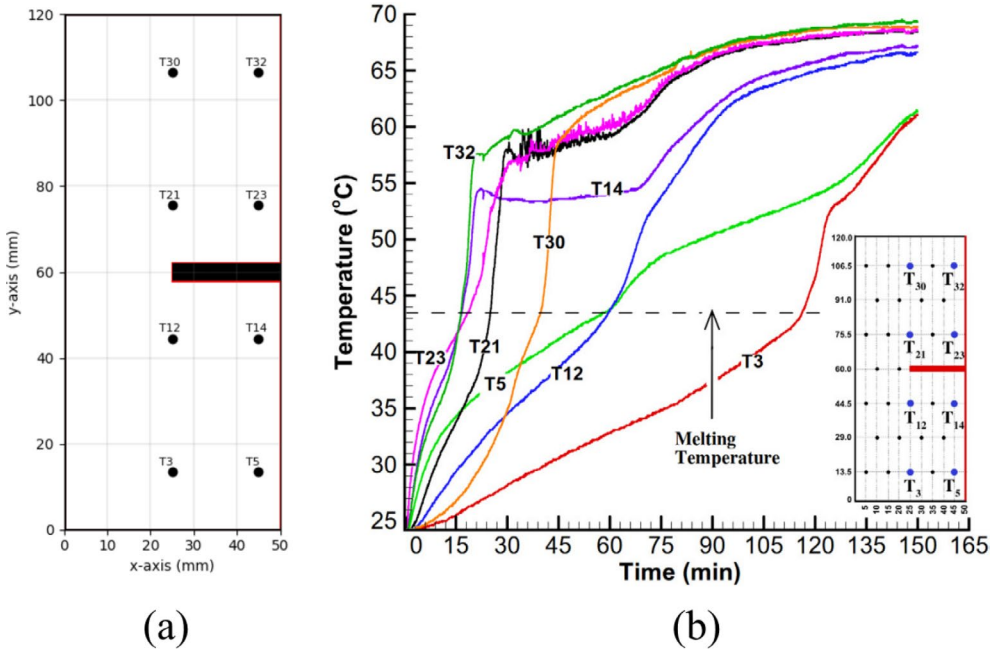

FIGURE 11 | Thermocouples measurement: (a) Measurement points location; (b) Temperature history from Kamkari and Shokouhmand [16].

points located above the fins, indicative of a higher rate of heat transfer at the solid–liquid interface adjacent to the fins. This behavior demonstrates the enhanced thermal performance afforded by the fins.

Upon reaching the simulated melting temperature, fluctuations occur, indicative of the solid-to-liquid phase transition. Consistent with experimental observations, the numerical simulations demonstrate decreasing temperatures along the vertical columns, a phenomenon attributed to the growth of the thermal boundary layer and the decreasing temperature of the liquid PCM in the lower regions of the enclosure. Furthermore, transient temperature fluctuations are observed in the simulations above the fins, mirroring the chaotic and vortical flow structures observed experimentally. These fluctuations diminish with proximity to the heated wall and decrease as the interface above the fins recedes, eventually leading to the formation of larger, stable vortices. The numerical results also capture the development of thermal stratification within the enclosures toward the completion of the melting process. The simulated temperatures clearly delineate a thermal layer, with diminishing convection currents in the upper regions as melting concludes. In finned enclosures, the simulations confirm that thermal stratification is confined to specific regions, such as the lower

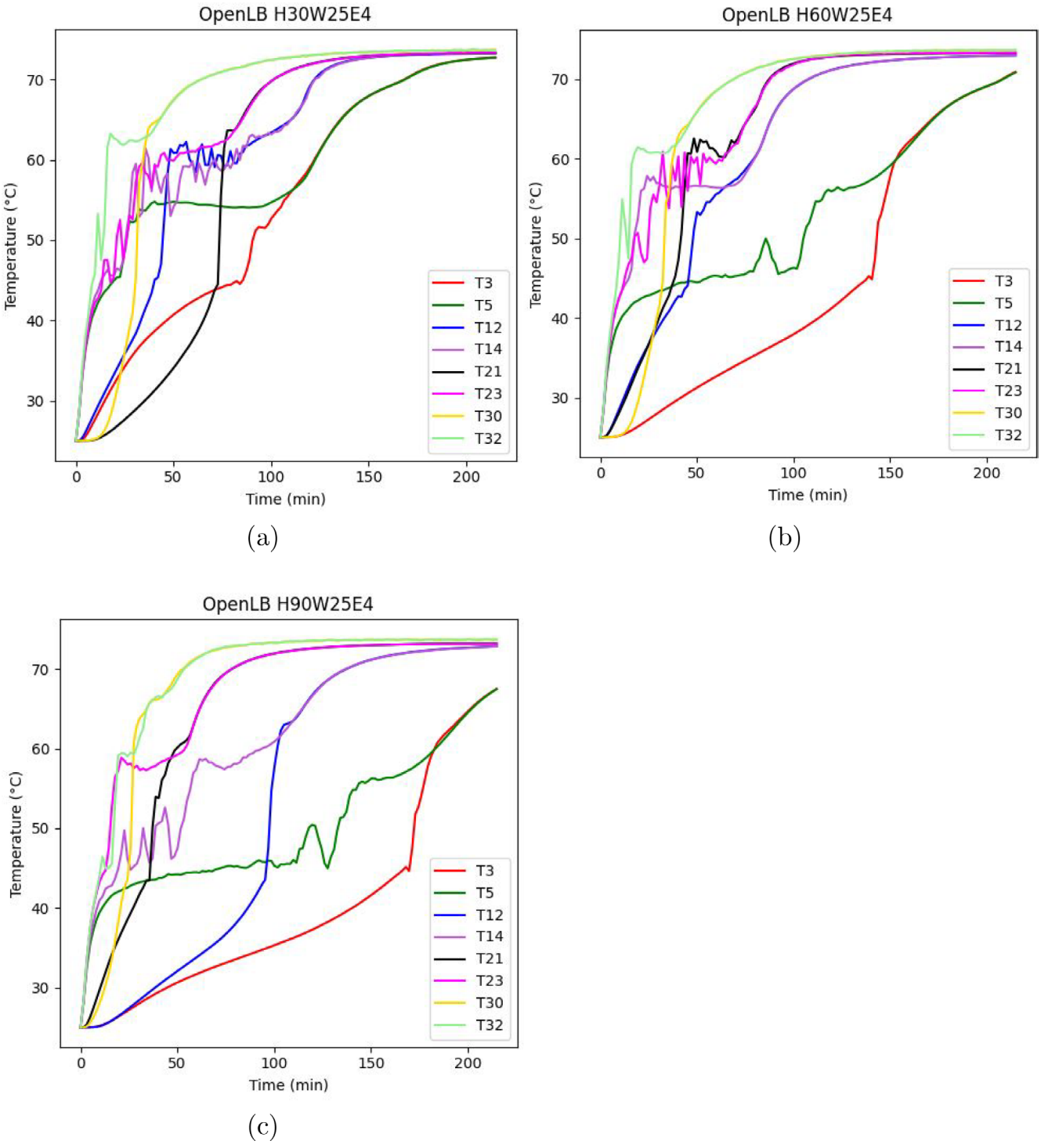

FIGURE 12 | Temperature at Tn location versus time: OpenLB results.

section of the enclosure, while mixing occurs in the regions above the fin surface. At locations T3 and T5, the fin's position within the cavity significantly influences the temperature response. In the lower cavity (H30), the material attains higher temperatures considerably faster than in the higher cavity positions (H60, H90). The closer the fin is to T3 and T5, the more efficient the heat transfer, accelerating the temperature rise and reducing the time required to reach higher temperatures. This is reflected in the faster heating rates and quicker stabilization times observed for the lower cavity configurations (H30).

Beyond the contributions to material behavior analysis, the primary focus of this study is the application of the Lattice Boltzmann Method (LBM) for investigating phase change processes in the selected material. The choice of LBM is motivated by its intrinsic advantages in handling complex boundary conditions, parallelization efficiency, and straightforward implementation of fluid–solid interactions, which are essential for accurately modeling the phase change processes, especially melting. Compared to traditional Navier–Stokes solvers, LBM offers a more efficient approach for simulating multiphase

flows, for it does not require complex meshing. However, it is important to acknowledge certain limitations, such as the need for fine lattice resolutions to capture sharp interfaces accurately and the potential for numerical diffusion in high-Rayleigh-number flows.

5 | Conclusion

A new OpenLB case using the Lattice Boltzmann Method was validated against experimental [16] and numerical [13] data, accurately modeling the melting behavior of lauric acid in a rectangular cavity. More specifically, this validation confirms its agreement in terms of the melting rates, total melting time, and the overall thermal response for the proposed TES. The LBM formulation accurately captures the most important phase change phenomena, producing results that correctly represent the major attributes of the expected physics.

Furthermore, the validated model was employed to conduct a parametric study investigating the influence of fin geometry—aspect ratio and placement on—total melting times. Twelve different configurations were simulated, varying both the fin aspect ratio and its location along the vertical wall. The results show that fin design has an important effect on melting efficiency and total melting time. Fins with higher aspect ratios, meaning longer and thinner fins, significantly improved melting performance, especially when placed near the bottom of the cavity. In these configurations, the fins promote stronger convective currents by interacting with cooler, still solid PCM in the lower regions. Between the maximum and minimum melting times obtained, the overall difference is 63.7%, which represents the higher melting rate for the longer fins in the lower area of the cavity. Compared to upper fin placements, lower-position fins consistently maintained increased melting rates, with improvements ranging from 11% to 26% depending on the fin aspect ratio. In fact, higher melting rates were observed in longer and thinner fins for all positions studied, with improvements ranging from 1% to 25% depending on the position.

To address some limitations identified in this study, future research could focus on the behavior of other phase change materials (PCMs) with the Lattice Boltzmann Method. In addition, new models should improve the applicability of LBM models by incorporating spatially and temporally varying thermal properties, particularly in applications with significant thermal differences. To strengthen the reliability of the OpenLB simulations, further validations against experimental data are recommended to include a broader range of materials, temperatures, initial conditions, and boundary conditions. These validations would confirm the robustness of the model across more diverse scenarios.

Acknowledgments

This work was supported by grants from the Fundação de Amparo à Pesquisa do Estado do Rio Grande do Sul—FAPERGS [24/2551-0001392-0 and 23/2551-0001894-2], Conselho Nacional de Desenvolvimento Científico e Tecnológico—CNPq [314082/2021-2, 408154/2022-5, 440279/2022-4, 404319/2024-6, and 309465/2025-7]. The contribution of Dr. Luiz Eduardo Czelusniak was supported by the Alexander von Humboldt Foundation through a Humboldt Research Fellowship. The authors gratefully acknowledge the computing time provided on the high-performance computer HoreKa by the National High-Performance Computing Center at KIT (NHR@KIT). This center is jointly supported by the Federal Ministry of Education and Research and the Ministry of Science, Research, and the Arts of Baden-Württemberg, as part of the National High-Performance Computing (NHR) joint funding program (https://www.nhr-verein.de/en/our-partners). HoreKa is partly funded by the German Research Foundation (DFG). The Article Processing Charge for the publication of this research was funded by the Coordenação de Aperfeiçoamento de Pessoal de Nível Superior - Brasil (CAPES) (ROR identifier: 00x0ma614).

Conflicts of Interest

The authors declare no conflicts of interest.

Data Availability Statement

The data that support the findings of this study are available from the corresponding author upon reasonable request.

References

1. M. J. Krause, A. Kummerländer, S. J. Avis, et al., "Openlb–Open Source Lattice Boltzmann Code," *Computers & Mathematics With Applications* 81 (2021): 258–288.

2. A. Kummerländer, F. Bukreev, S. Berg, M. Dorn, and M. Krause, "Advances in Computational Process Engineering Using Lattice Boltzmann Methods on High Performance Computers for Solving Fluid Flow Problems," *High Performance Computing in Science and Engineering* 22 (2022): 233–247.

3. V. Heuveline, M. J. Krause, and J. Latt, "Towards a Hybrid Parallelization of Lattice Boltzmann Methods," *Computers & Mathematics with Applications* 58, no. 5 (2009): 1071–1080.

4. A. Laouer, K. Al-Farhany, M. F. Al-Dawody, and A. L. Hashem, "A Numerical Study of Phase Change Material Melting Enhancement in a Horizontal Rectangular Enclosure With Vertical Triple Fins," *International Communications in Heat and Mass Transfer* 137 (2022): 106223.

5. R. Dai, Q. Bian, Q. Wang, and M. Zeng, "Evolution of Natural Convection Melting Inside Cavity Heated From Different Sides Using Enthalpy Based Lattice Boltzmann Method," *International Journal of Heat and Mass Transfer* 121 (2018): 715–725.

6. R. Dai, X. Lu, X. Tong, and J. Deng, "Thermal Performance Analysis of Different t-Shaped Fin Configurations on Thermal Energy Storage Through Simplified Enthalpy Based Lattice Boltzmann Method," *Case Studies in Thermal Engineering* 53 (2024): 103861.

7. F. Talati and M. Taghilou, "Lattice Boltzmann Application on the Pcm Solidification Within a Rectangular Finned Container," *Applied Thermal Engineering* 83 (2015): 108–120.

8. R. Mabrouk, H. Dhahri, H. Naji, S. Hammouda, and Z. Younsi, "Lattice Boltzmann Simulation of Forced Convection Melting of a Composite Phase Change Material With Heat Dissipation Through an Open-Ended Channel," *International Journal of Heat and Mass Transfer* 153 (2020): 119606.

9. Y. Feng, H. Li, L. Li, L. Bu, and T. Wang, "Numerical Investigation on the Melting of Nanoparticle-Enhanced Phase Change Materials (Nepcm) in a Bottom-Heated Rectangular Cavity Using Lattice Boltzmann Method," *International Journal of Heat and Mass Transfer* 81 (2015): 415–425.

10. M. Hosseini, A. Ranjbar, M. Rahimi, and R. Bahrampoury, "Experimental and Numerical Evaluation of Longitudinally Finned Latent Heat Thermal Storage Systems," *Energy and Buildings* 99 (2015): 263–272.

11. C. Ji, Z. Qin, S. Dubey, F. H. Choo, and F. Duan, "Simulation on Pcm Melting Enhancement With Double-Fin Length Arrangements in a Rectangular Enclosure Induced by Natural Convection," *International Journal of Heat and Mass Transfer* 127 (2018): 255–265.

12. A. Abdi, V. Martin, and J. N. Chiu, "Numerical Investigation of Melting in a Cavity With Vertically Oriented Fins," *Applied Energy* 235 (2019): 1027–1040.

13. R. D. C. Oliveski, F. Becker, L. A. O. Rocha, C. Biserni, and G. E. S. Eberhardt, "Design of Fin Structures for Phase Change Material (Pcm) Melting Process in Rectangular Cavities," *Journal of Energy Storage* 35 (2021): 102337.

14. M. Siodlaczek, M. Gaedtke, S. Simonis, M. Schweiker, N. Homma, and M. J. Krause, "Numerical Evaluation of Thermal Comfort Using a Large Eddy Lattice Boltzmann Method," *Building and Environment* 192 (2021): 107618.

15. M. Gaedtke, S. Abishek, R. Mead-Hunter, et al., "Total Enthalpy-Based Lattice Boltzmann Simulations of Melting in Paraffin/Metal Foam Composite Phase Change Materials," *International Journal of Heat and Mass Transfer* 155 (2020): 119870.

16. B. Kamkari and H. Shokouhmand, "Experimental Investigation of Phase Change Material Melting in Rectangular Enclosures With Horizontal Partial Fins," *International Journal of Heat and Mass Transfer* 78 (2014): 839–851.

17. R. D. C. Oliveski, A. de Quadro Tacques Filho, and I. A. Schröer, "Melting and Solidification in Thermal Storage: Influence of Fin Aspect Ratio and Positioning in a Full Charging and Discharging Cycle," *Journal of Energy Storage* 50 (2022): 104303.

18. T. Krüger, H. Kusumaatmaja, A. Kuzmin, O. Shardt, G. Silva, and E. M. Viggen, The Lattice Boltzmann Method (2017).

19. R. Huang, H. Wu, and P. Cheng, "A New Lattice Boltzmann Model for Solid–Liquid Phase Change," *International Journal of Heat and Mass Transfer* 59 (2013): 295–301.

20. R. Huang and H. Wu, "Phase Interface Effects in the Total Enthalpy-Based Lattice Boltzmann Model for Solid–Liquid Phase Change," *Journal of Computational Physics* 294 (2015): 346–362.

21. J. Lu, H. Lei, and C. Dai, "An Optimal Two-Relaxation-Time Lattice Boltzmann Equation for Solid-Liquid Phase Change: The Elimination of Unphysical Numerical Diffusion," *International Journal of Thermal Sciences* 135 (2019): 17–29.

22. D. R. Noble and J. R. Torczynski, "A Lattice-Boltzmann Method for Partially Saturated Computational Cells," *International Journal of Modern Physics C* 09, no. 8 (1998): 1189–1201.

23. S. Hou, J. Sterling, S. Chen, and G. Doolen, "A Lattice Boltzmann Subgrid Model for High Reynolds," *Pattern Formation and Lattice Gas Automata* 6, no. 6 (1996): 151.

24. M. Gaedtke, S. Wachter, M. Raedle, H. Nirschl, and M. J. Krause, "Application of a Lattice Boltzmann Method Combined With a Smagorinsky Turbulence Model to Spatially Resolved Heat Flux Inside a Refrigerated Vehicle," *Computers & Mathematics with Applications* 76, no. 10 (2018): 2315–2329.

Supporting Information

Additional supporting information can be found online in the Supporting Information section. **Video S1:** Lauric acid simulation under the melting process with OpenLB.